

Development of algorithms for the end-end system simulation and performance analysis for a high-frequency magnetic diagnostic system: application to ITER, JET and TCV

D.Testa¹, G.Ambrosino^{2*}, M.Ariola², G.deTommasi², A.Pironti², the TCV team^a, JET contributors^b

¹*Ecole Polytechnique Fédérale de Lausanne (EPFL), Swiss Plasma Center (SPC), CH-1015 Lausanne, Switzerland*

²*Consorzio CREATE, 80125 Napoli, Italy*

**this contribution is in fond memory of the late Prof. Giuseppe "Peppe" Ambrosino, who has always been very supportive and very instrumental in the progress of this work*

Corresponding author: Duccio Testa (duccio.testa@epfl.ch)

An innovative and very detailed end-to-end system modelling tool has been developed and applied to test on simulated data the actual measurement capabilities of any generic high frequency (HF) magnetic diagnostic systems. The main goal of this rather complex tool is to obtain estimates of the intrinsic measurement uncertainties and then assess the actual vs. intended system measurement performance for *correctly detecting* individual components in the frequency spectrum of HF magnetic instabilities in the plasma. This has paramount consequences not solely for off-line analyses but also, and more importantly, for any real-time application where, as an example, the mode frequency, amplitude and {toroidal, poloidal} mode numbers are used to determine whether, and which, corrective actions need to be taken to stabilize the discharge.

The algorithm has been applied to some of the various ITER HF magnetic diagnostic systems, most notably the AJ (LTCC-1D sensors) system as currently designed, hence providing specific confidence levels and error bounds for detecting the modes highlighted in the ITER measurement specifications. Additional analyses have been performed for the TCV and JET HF magnetic diagnostics, providing further constraints on the results obtained with these systems.

Keywords: magnetic diagnostic, high-frequency measurements, SparSpec code

^a See the author list of H.Reimerdes et al., Nucl. Fusion 62 042018 (2022).

^b See the author list of "Overview of JET results for optimising ITER operation" by J.Mailloux et al., to be published in Nuclear Fusion Special issue: Overview and Summary Papers from the 28th Fusion Energy Conference (Nice, France, 10-15 May 2021).

1) Introduction.

High frequency (HF) magnetic measurements (δB_{MEAS}) are needed to monitor instabilities which may become detrimental to the overall plasma confinement and thus the fusion performance. These δB_{MEAS} data are now routinely interfaced with real-time (RT) control systems to produce observables that appropriate actuators can then modify to desired values. This approach works well only if the performance of the measurement system is known precisely and is correctly considered in the RT control schemes. Therefore, it is paramount to determine error bounds and confidence level off-line on the RT observables. This is best done by using end-to-end system simulations, thus essentially developing a synthetic diagnostic for the δB_{MEAS} data, *because in this case one is certain of what the results of the analysis should be*. Then one can indeed attempt to control on-line magnetic fluctuations using the correct knowledge basis for the measurement accuracy: *one should NOT control anything beyond that!*

An overall description of an HF magnetic diagnostic system can be found in the recent tutorial paper published in Review of Scientific Instruments (see ref.[1], and specifically the Supplemental Material section and the many references therein for further and more detailed information). The Readers are referred to this publication for relevant information not directly provided here. On the other hand, a modern tutorial and general introduction on the interface between an HF magnetic diagnostic system and an RT system is not readily available in the literature. Reference [2] provide some insights on the hardware interface and some potential applications of such an RT system. The most useful introduction on the need for error estimates also for RT analyses is provided by the (unpublished) ITER measurement specifications for the HF magnetic diagnostic system [3] and by the (unpublished as well) contract specifications for the ITER RT software for HF mode analyses [4], of which all the Authors of this paper were contributors.

This end-to-end modelling tool has been initially applied on simulated data extracted from a large database of magnetic instabilities observed in the TCV tokamak [1], which include relatively low frequency Tearing Modes in the frequency range from $\sim 1\text{kHz}$ to $\sim 10\text{kHz}$, fishbones and sawbones in the frequency range from $\sim 10\text{kHz}$ to $\sim 30\text{kHz}$, Geodesic Acoustic Modes, Alfvén Eigenmodes and more generally Energetic Particle Modes in the range $\sim 50\text{kHz} \rightarrow 1\text{MHz}$. In this work we now extend the application of this algorithm to the existing HF magnetic diagnostic system in JET and to the ITER AJ (localized: LTCC-1D sensors) HF magnetic diagnostic system, as currently designed. When then using actual data from the HF magnetic diagnostic systems available on these tokamaks, this allows testing the intended vs. the actual measurement performance and the RT control stability and effectiveness for these instabilities, precisely because the error bounds on the measurements are known a-priori and can then be correctly considered in RT.

This paper is organized as follows. In Section-2 we briefly review the mathematical approach of our end-to-end system modelling tool: all relevant details are provided in Section-I of the Supplemental Material of [1]. Section-3 to Section-5 present the results of the simulations performed for the TCV, JET and finally ITER tokamaks. Section-6 presents our summary conclusions and an overview of the ongoing work, specifically aimed at making this tool more user-friendly so that it could easily be deployed for other tokamaks such as DTT and DEMO.

2) A synthetic diagnostic for the δB_{MEAS} data: the mathematical background.

The mathematical approach used to construct the δB_{MEAS} data for each sensor in each device has been extensively presented in Section-I of the Supplemental Material of [1], and thus it is only very briefly reviewed here for clarity of presentation.

To perform the end-to-end simulation of any HF magnetic diagnostic system, we need to generate the δB_{MEAS} data as a time series, and this is most easily done directly at the sensors' position. This scheme is then completely independent of which class of modes is being considered and corresponds exactly to what is measured by a blind diagnostic as it does not require any prior knowledge of the plasma configuration (equilibrium, resonant surface for the modes, position of the Last Closed Flux Surface (LCFS), ...). Therefore, $\delta B_{MEAS,l}(t_p)$ is constructed for each magnetic sensor l at each time-point t_p as an integral over the whole frequency spectrum of all its frequency components:

$$\delta B_{MEAS,l}(t_p) = \int_{-\infty}^{+\infty} d\omega \left\{ S_{CONT}(\omega, t_p) + \varepsilon_l(\omega, t_p) + \sum_{k=1}^K A_k \exp(-i\omega_k t_p) \exp(-in_k \phi_l - im_k \theta_l) \right\} * TF_{H,l}(i\omega) \quad (1)$$

In eq.(1) $S_{CONT}(\omega, t_p)$ is the frequency-dependent background continuum spectrum, which is assumed to be the same for all sensors, $\varepsilon_l(\omega, t_p)$ is the noise spectrum, individualized for each sensor, K is the maximum number of individual modes included in the analysis, each of them having angular frequency $\omega_k = 2\pi f_k$, and toroidal and poloidal mode numbers n_k and m_k , respectively. Finally, $TF_{H,l}(i\omega)$ is the analogue Transfer Function (TF) for the end-to-end acquisition line in the Laplace $s=i\omega$ domain. Using the toroidal coordinate system (R, Z, ϕ) and defining α as the angle between the measurement axis of the sensor and the normal to the LCFS, the $\delta B_{MEAS,l}(t_p)$ data of eq.(1) are then individualized for each sensor at $(R_l, Z_l, \phi_l; \alpha_l)$ by:

- $(R_l, Z_l, \phi_l) \rightarrow$ adding the equilibrium magnetic field at the position of the sensor;
- $(R_l, Z_l, \phi_l) \rightarrow$ implementing the toroidal and poloidal dependencies for each mode;
- $(\alpha_l) \rightarrow$ projecting the signal onto the measurement axis of the sensor;
- $\varepsilon_l(\omega, t_p) \rightarrow$ using the noise components specific to that sensor at the time point t_p ;

- $TF_{H,l}(i\omega) \rightarrow$ implement the end-to-end frequency-dependent analogue transfer function of the acquisition line specific to that sensor.

There is a specific peculiarity for the saddle loops (or any other extended sensor): a 2D integral is performed over the $\{Z,\phi\}$ -range covered by that sensor. This does not apply to sufficiently small sensors, for which the measurement is assumed to be localized, thus the simulated data do not need to be spatially integrated.

The $\delta B_{MEAS,l}$ data must account for $TF_{H,l}(i\omega)$ as the hardware changes $\{A\}$ (here the notation $\{x\}$ indicates an ensemble of the elements x) and introduces time delays which affect the determination of $\{n, m\}$; the mode frequencies $\{f\}$ are essentially un-affected by the hardware. For the calibration of the δB_{MEAS} data two very important points must be noted (see [1] for further details):

- hardware: the transfer function $TF_H(s=i\omega)$ is in the Laplace domain and is a continuous function of $\omega \in [-\infty, +\infty]$;
- digital (software) calibration: the transfer function $TF_C(z)$ is in the digital domain $z=e^{s\tau}$, τ being the DAQ sampling time, therefore it is a periodic function in the domain defined by $f \in [0, 1/\tau]$ and must be inverted, giving $invTF_C(z)$, to obtain the ensemble of $\{n, m, A\}$ for each mode from a suitably selected ensemble of $\{\delta B_{MEAS}\}$ for the set of measured mode frequencies $\{f\}$.

This can then be formulated as follows, where the symbol @ means *applied to*:

$\{n, m, A\}(t)=invTF_C(z)@\{\delta B_{MEAS}(t,\{f(t)\})\}.$	(2)
--	-----

The mapping $TF_H(s) \rightarrow invTF_C(z)$ is in general specific for each sensor (as one cannot guarantee that all end-to-end acquisition lines would be the same, namely at least they must differ by the randomized combination of the manufacturing tolerances for each specific hardware component) and therefore always introduces further frequency-dependent uncertainties in determining the ensemble of $\{n, m, A\}$, which must therefore be correctly accounted for.

To determine the ensemble of mode frequencies $\{f\}$, we use a parametric Auto-Regressive (AR) Power Spectral Decomposition (PSD) method, as the usual Fast Fourier Transform (FFT) can be very noisy at higher frequencies and/or when a very fine FFT frequency grid is used without adequate windowing (see fig1 for a typical example of this). Then a high-resolution FFT is performed around the frequencies determined using the PSD-AR method: this gives a complex signal as function of the sensor position. This signal can then be spatially decomposed to obtain the toroidal and poloidal mode numbers, and the corresponding FFT mode amplitudes. The spatial analysis is performed comparing three different methods in our system simulations:

- 1) for sensors in a purely 1D {toroidal, poloidal} arrangement, we use the Linear Phase Fit (LPF) method, which perform a linear fit on the phase of the complex FFT signal;

- 2) also for sensors in a purely 1D {toroidal, poloidal} arrangement, we use the SparSpec-H2 (SS-H2) [5] method, which uses the full complex FFT signal (amplitude and phase);
- 3) for sensors which are in a 2D arrangement, we use the SparSpec-2D (SS-2D) algorithm [6], again applied to the full complex FFT signal (amplitude and phase).

In summary, we generate for each sensor an individualized, frequency-calibrated time series using a combination of a continuous spectrum S_{CONT} , with spectral breaks where the power-law exponent α for $S_{\text{CONT}} \sim \text{freq}^\alpha$ changes value (see [1] for further details on this), various modes, various sources of coloured (frequency-dependent) noise ε normalized to contain a certain fraction of the total energy content in the continuous part of the input signal. The time series is then analysed, so that the output values $\{f, n, m, A\}_{\text{OUT}}$ can be compared to the corresponding input values for the mode frequency, amplitude, toroidal and poloidal mode numbers. The analysis is then repeated over a certain number of simulations (typically at least 100) varying S_{CONT} , ε and $\{A\}_{\text{IN}}$ for a fixed set of $\{f, n, m\}_{\text{IN}}$. This provides the RMS and STD values on $\{f, n, m, A\}_{\text{OUT}}$ and thus allows to determine the overall success of the simulation for the same set of $\{f, n, m, A\}_{\text{IN}}$, labelled *score*. Note that the simulation score is dependent on the specific spatial analysis method deployed for the analysis. For each time window in the analysis, the score is set to be =1.00 for perfect detection within the intrinsic measurement errors for the specific HF magnetic diagnostic system, which are linked to positional errors and tolerances on the hardware components (*obviously, one cannot do better than what the measurement system allows*). The score is then penalized as the square root of the sum of the squares of the relative difference in the frequency and amplitude for each {toroidal, poloidal} mode. A further penalization is added to account for the bi-directional number of *missed* modes, namely the output (respectively input) modes which are NOT correspondingly present in the input (respectively output) signal. The score can therefore also be seen as a criterion for failure in mode detection: the lower the score, the higher the failure rate in correctly detecting the mode.

Figure1 shows an example of such a time series for one of the ITER AJ sensors. For this simulation, three modes at $f_{\text{IN}}(@t=0) = \{15 \pm 5, 25 \pm 0.1, 35 \pm 3\}$ kHz are used, with varying frequency (hence the \pm symbols) and amplitude over the 35msec time-window of the simulation. The modes have fixed $\{m/n\}_{\text{IN}} = \{3/2, 4/3, 5/3\}$. The noise is pink, namely with spectral power density $\sim 1/f$ without spectral breaks and has a relative energy content =0.05; a continuum spectrum with a Kolmogorov power law [7] scaling for the spectral density $\sim f^{-5/3}$ is used, also without spectral breaks.

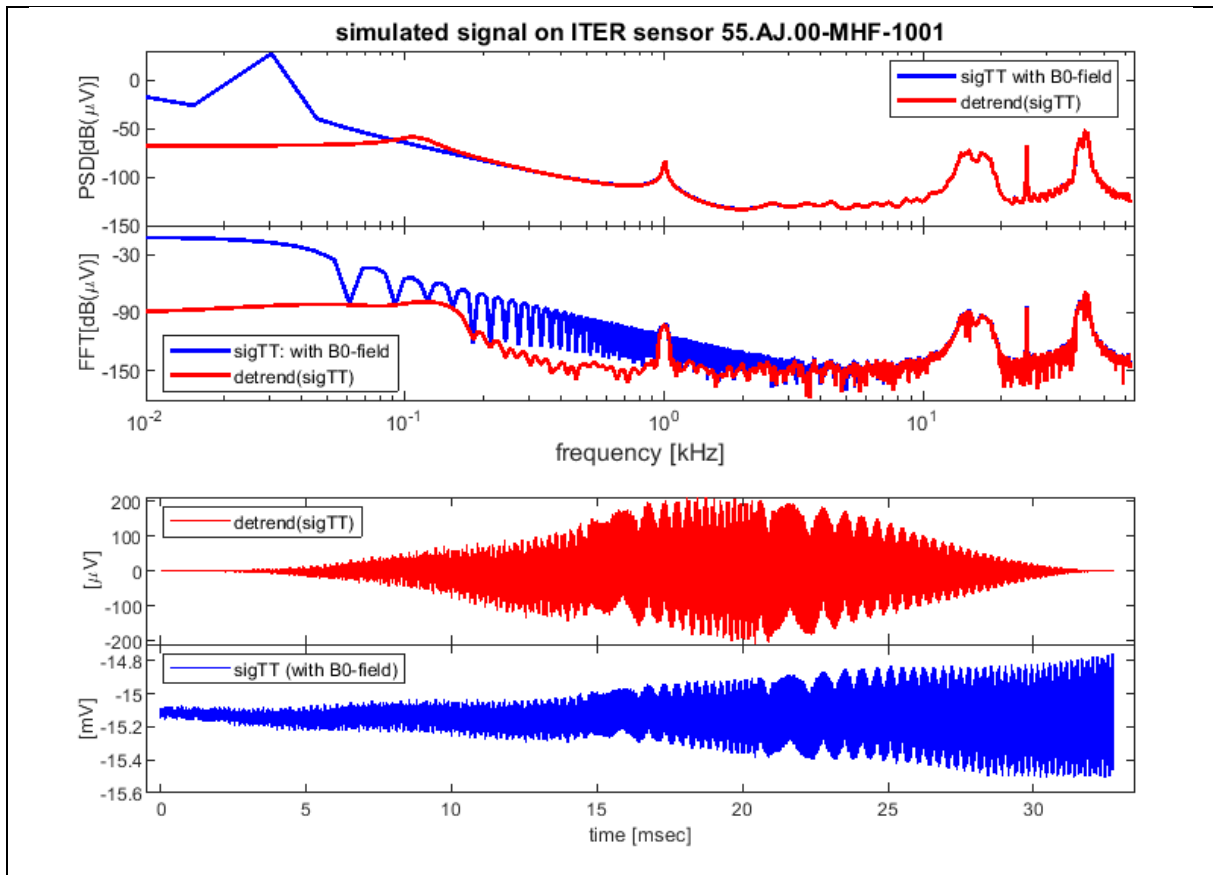


Figure 1. The time series generated for one of the ITER AJ sensors. Note the 1kHz signal due to the DAQ sampling scheme. The signal is with (blue) and without (red) the equilibrium magnetic field, which is removed using a simple detrending scheme. In the top two frames, we show the FFT and PSD-AR frequency analysis of the entire time series: note the much higher noise in the FFT data. The frequency and amplitude variation of the modes explains why the FFT and PSD are not a δ -function at the modes' frequency. The larger width of the lowest and highest frequency modes is due to a much larger amplitude and frequency variation during the time window of the simulation. The ITER DAQ sampling frequency is 2MHz, but for clarity of illustration the frequency spectrum is only plotted up to 50kHz.

3) A synthetic diagnostic for the δB_{MEAS} data: the TCV case.

The TCV tokamak is exceptionally well equipped with HF magnetic sensors [8, 9]: we have indeed 206x localised Mirnov-1D coils, 3x localised LTCC-3D probes and 24x extended saddle loops distributed in various arrays on the low- and high-field-side (LFS, HFS) at different vertical heights with respect to the geometric centre of the tokamak at $\{R_0=0.88\text{m}, Z_0=0\text{m}\}$. Figure 2 shows the position of the Mirnov and LTCC-3D magnetic sensors. Note that the LTCC-3D data are acquired at 2MHz, while the Mirnov data are acquired at 500kHz, which makes it not very straightforward to use these two systems together.

Figure 3 shows the summary results of the TCV simulations performed for a single $\{n, m\}_{IN}$ mode at $f_{IN}=10\text{kHz}$, with varying $\{n, m, A\}_{IN}$ and running 100 simulations, in this case neglecting the further errors due to difference in the calibration and noise pick-up for the different sets of sensors. For the toroidal analyses (fig 3a), we use the arrays LFS-TOP (all sensors located at the poloidal position =17), HFS-MID (all sensors located at the poloidal position =1), and LFS-MID (all sensors nominally

located at the poloidal position $\theta=20$, but two sensors were displaced at the poloidal position $\theta=21$ to accommodate the Neutral Beam Injection system). For the poloidal analyses (fig3b), the LPF and SS-H2 1D methods are deployed on the 11x poloidal sensors on the LFS, labelled 15 \rightarrow 25 in the poloidal cross-section of fig1, and here dubbed *POL-LFS* for simplicity. For the SS-2D analysis, we use a combination of LFS, HFS, POL and the 3x LTCC sensors.

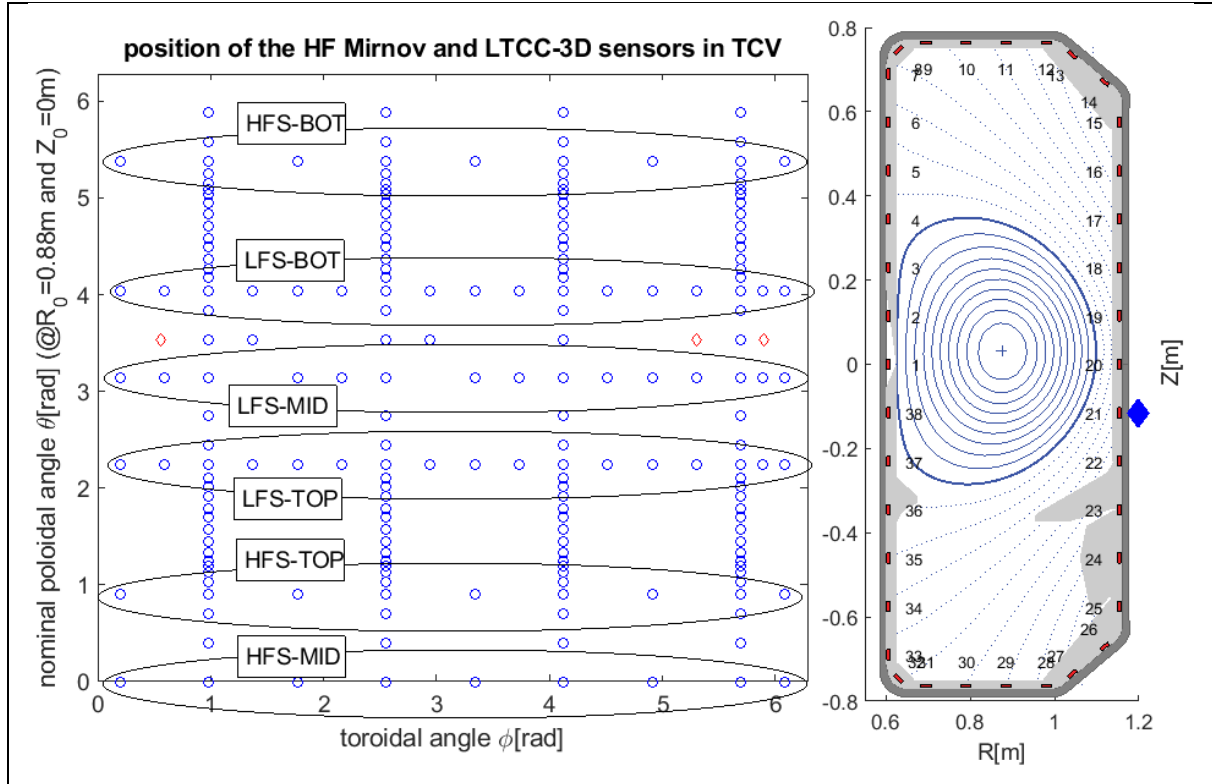


Figure2. A schematic layout of the distribution of the HF magnetic sensors in TCV, highlighting the naming convention for the 6x different toroidal arrays used for the analyses. In the left frame vs. the angular coordinates $\{\phi, \theta\}$, blue circles are the 206x Mirnov, red diamonds are the 3x LTCC-3D. In the right frame vs. $\{R, Z\}$, the blue diamond indicating the poloidal position of the LTCC-3D sensors has been slightly displaced outwards for clarity of plotting, as otherwise it would overlap with the Mirnov sensor #21. The magnetic surfaces for one representative TCV discharge are also shown to illustrate the position of the sensors with respect to the LCFS. The wall (where the sensors are mounted) is NOT conformal to the LCFS, and this much complicates the analyses of poloidal mode numbers.

For the poloidal-1D analyses, we note that the best results are obtained using the LPF method on the POL-LFS array, while for the toroidal-1D analysis the SS-H2 and LPF methods perform equivalently well but only up to $|n|=8$ on the LFS and $|n|=4$ on the HFS. The SS-2D analyses are clearly NOT very useful in TCV. These results are due to the specific sensors' arrangement in TCV, where essentially orthogonal arrays with equi-spaced sensors are deployed. As clear from fig2, an intrinsic $|n|=8$ (due to 16x equi-spaced sensors) and $|n|=4$ (due to 8x equi-spaced sensors) periodicity exists in the LFS and HFS arrays, respectively: this significantly compromises the analyses for higher mode numbers. Figure4 compares the results for a test $m/n=5/3$ Neoclassical Tearing Mode (NTM) as function of frequency. This NTM is observed in JET at around 35kHz, with a detrimental effect on confinement.

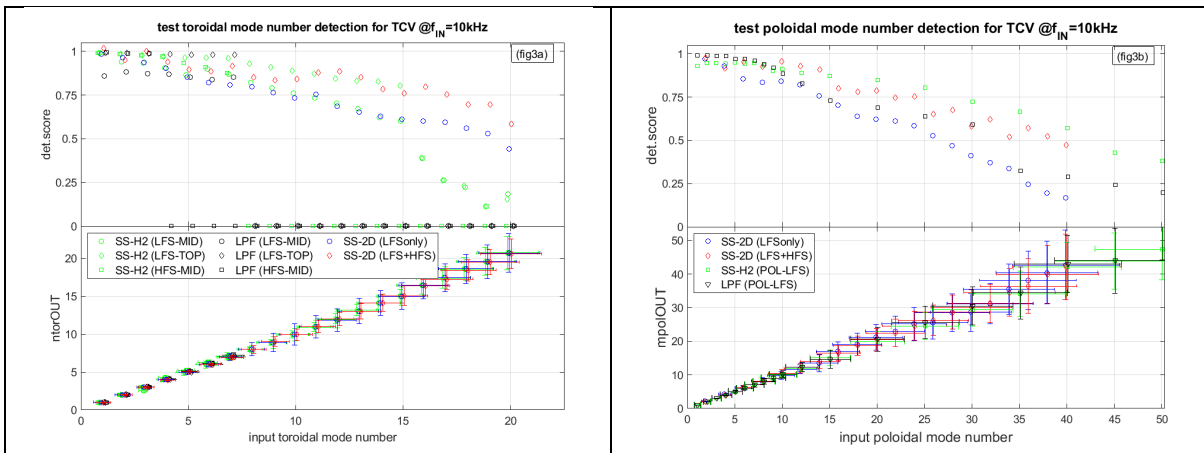


Figure3(a,b). Summary results of the system end-to-end simulation for TCV, using one single $\{n, m\}_{IN}$ mode at $f_{IN}=10\text{kHz}$ (left frame, fig3a: toroidal analysis; right frame, fig3b: poloidal analysis). The horizontal error bars on $\{n, m\}_{IN}$ mode numbers represent the intrinsic and unavoidable measurement uncertainty due to tolerances in the position of the sensors and in the hardware specifications. The vertical error bars on $\{n, m\}_{OUT}$ represent the scatter in the output data over the 100 simulations used for these analyses.

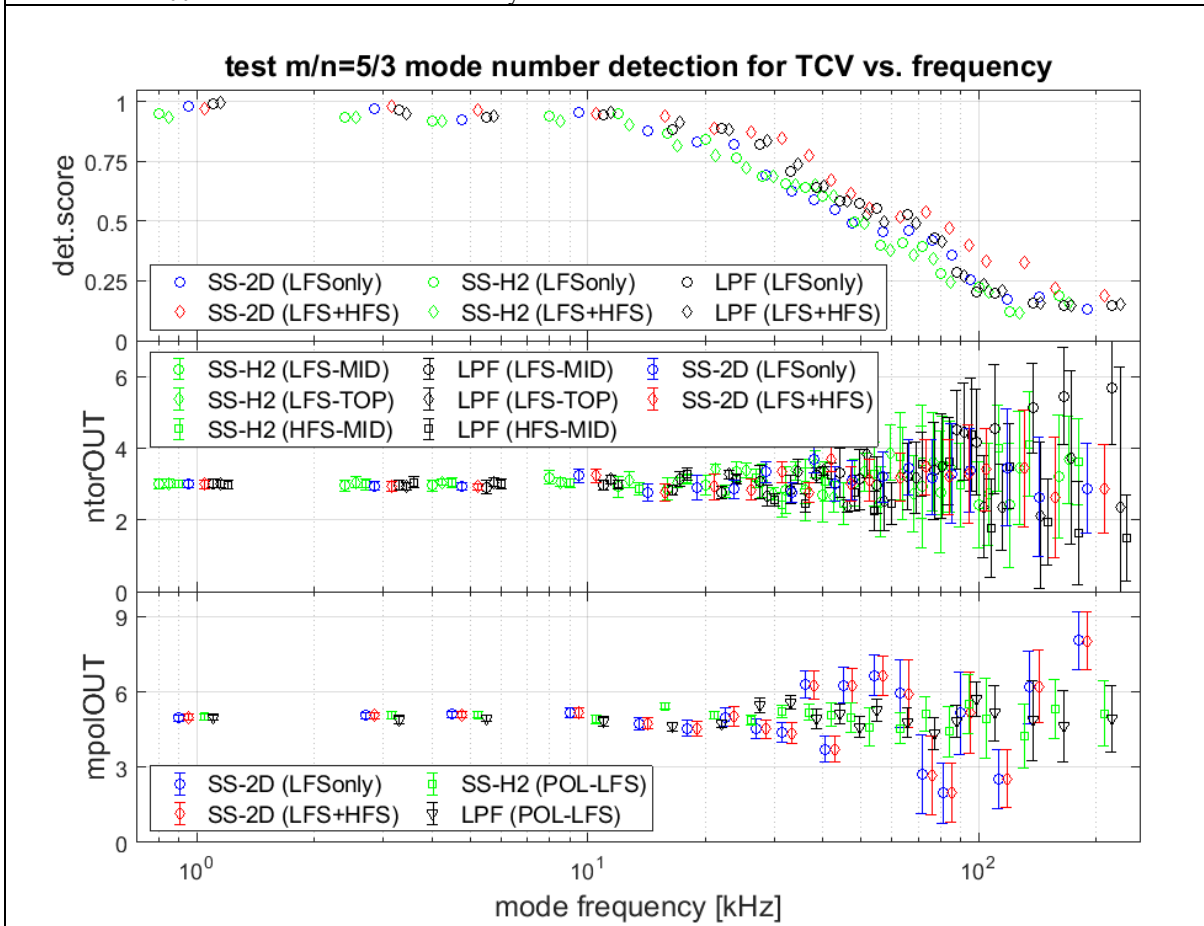


Figure4. Summary results of the system end-to-end simulation for TCV, using one single $\{m/n\}_{IN}=5/3$ mode for frequencies between 1kHz and 200kHz. Above $\sim 50\text{kHz}$ the detection score significantly decreases, because the TCV Mirnov sensors pick-up significant EM noise from different power supplies due to their complex grounding at different points along the acquisition line. Furthermore, most of the acquisition hardware has been installed around 25 years ago when a 10kHz sampling frequency was used. Some of the hardware is not optimized for higher frequencies and show significant ageing. This translates in rather different $T_F(s)$ for the different lines, particularly at higher frequencies $>50\text{kHz}$, which are then very difficult to cross-calibrate.

This mode is used as a reference not only for the JET analyses (see Section-4 below) but also for the TCV analyses to illustrate the role of frequency-dependent calibration errors and noise. For this analysis we do now include all sources of noise (as measured during dedicated back-off shots) and the calibration errors, namely those associated with the process of going from $TF_H(s)$ to $invTF_C(z)$ as highlighted by eq.(2) above, all terms individualized for each sensor. The detection score significantly decreases above $\sim 50\text{kHz}$, due to various sources of noise pick-up and a problematic cross-calibration between the different acquisition lines.

4) A synthetic diagnostic for the δB_{MEAS} data: the JET case.

Figure5 shows the position of the HF magnetic sensors in JET. Different sets of HF magnetic sensors exist, for purely toroidal (the T-coils, the poloidal coordinate being the same for all of them) and purely poloidal (the PP-coils, the toroidal coordinate being the same for all of them) analyses, sitting on the inner (just a few, the I-coils) and the outer (most of them) vessel walls. Some of these sensors are positioned very close to each other to form a high-resolution array (the H-coils) with 8 sensors.

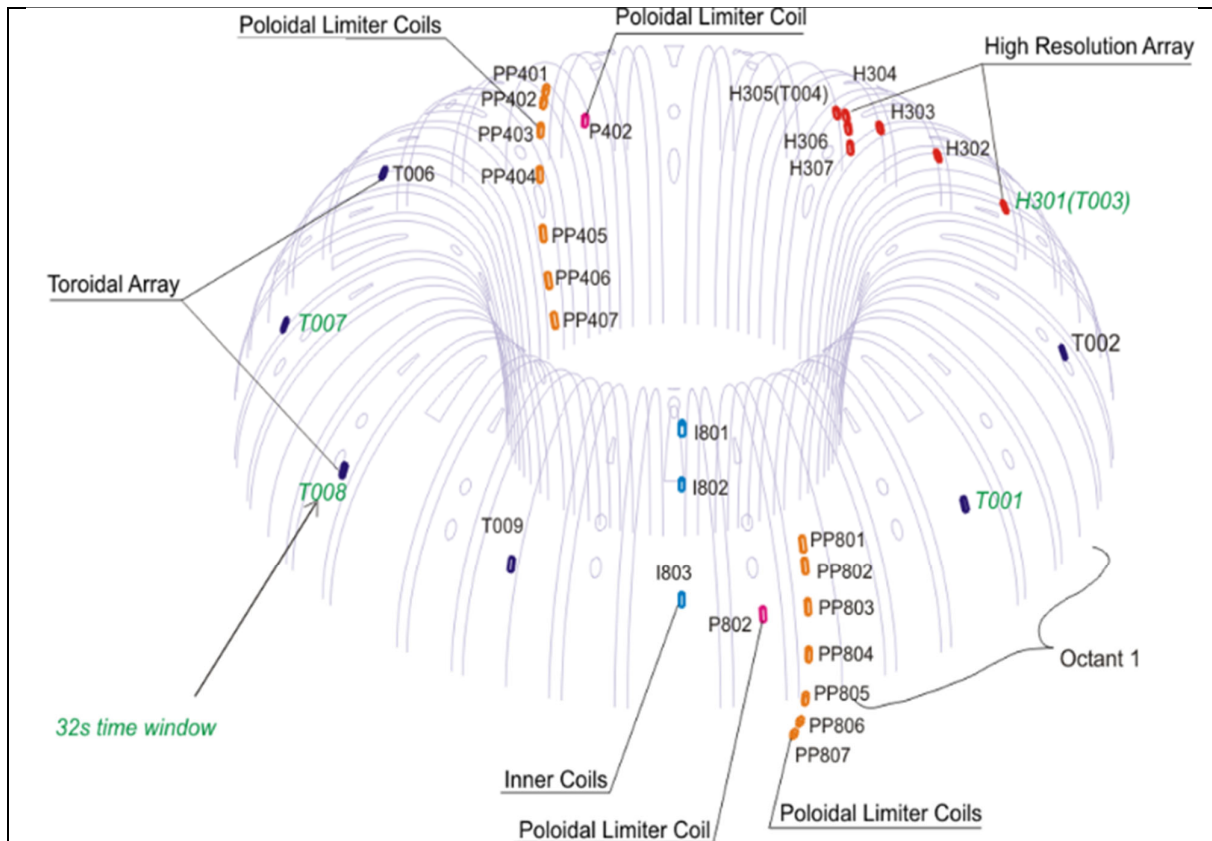


Figure5. A schematic layout of the distribution of the HF magnetic sensors in the JET tokamak, together with a 3D folded view of the inner and the outer vessel structure. In JET (and as expected in ITER, DTT, DEMO), the wall is usually conformal to the LCFS, therefore the poloidal mode number analyses are generally simpler than for TCV.

Figure6a and fig6b show the summary results of the JET simulations performed for a single $\{n, m\}_{IN}$ mode at $f_{IN}=10\text{kHz}$, with varying $\{n, m, A\}_{IN}$ and running 100 simulations.

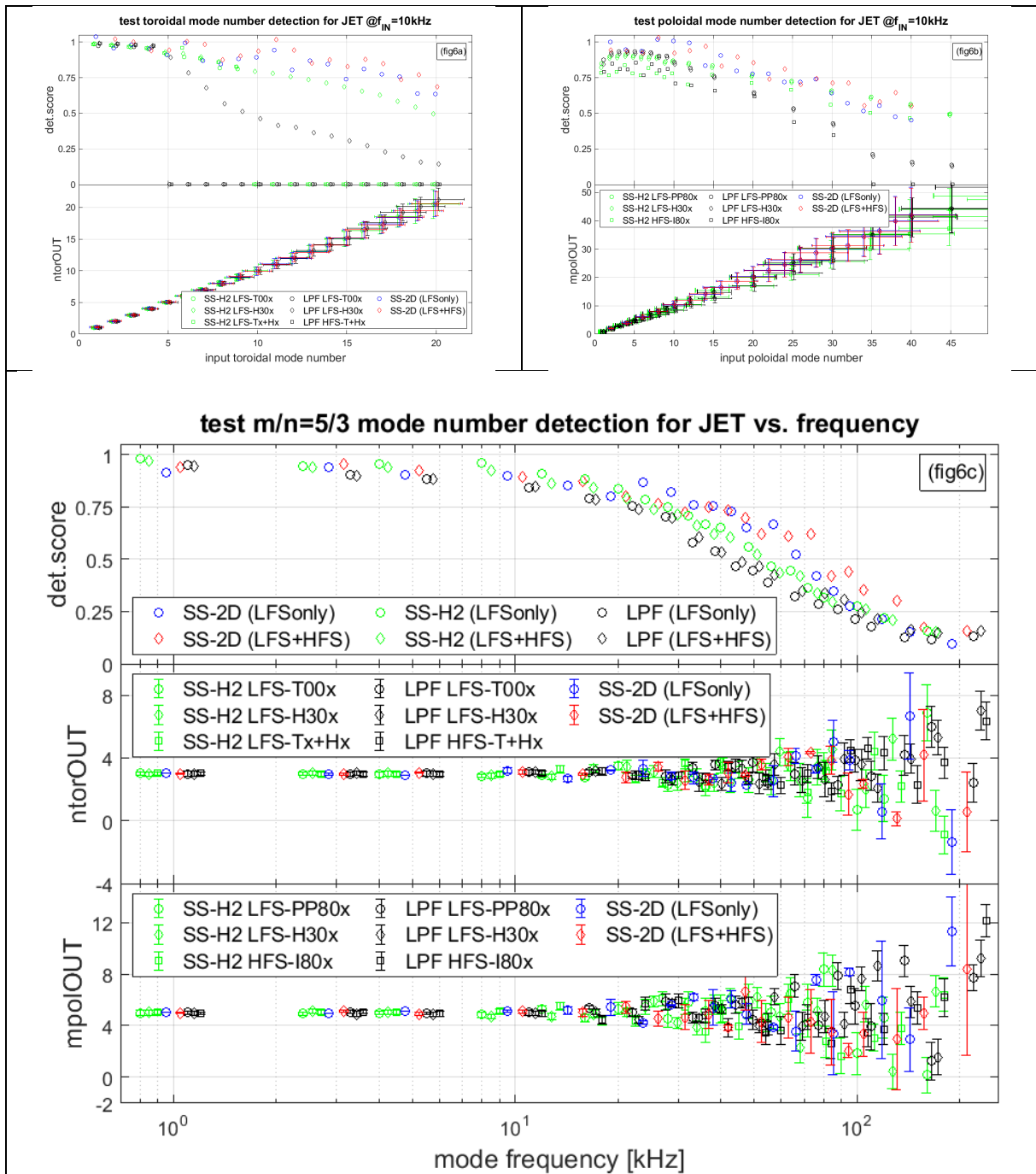


Figure6. On the top left (fig6a) and top right (fig6b) frames, using the same format as in fig3(a,b), the summary results for the toroidal and poloidal mode number detection as function of $\{n, m\}_{IN}$ at $f_{IN}=10\text{kHz}$, without considering noise pick-up and calibration: the detection is quite good, particularly for the SparSpec methods, up to $|m|\sim 20$ and $|n|\sim 10$. However, as clear from the bottom frame (fig6c), using the same format as in fig4), when considering the noise and calibration for a specific $m/n=5/3$ mode as function of frequency, the detection becomes quite poor already for frequencies above $\sim 50\text{kHz}$.

The results in fig6(a,b) are obtained neglecting the further errors due to difference in the calibration and noise pick-up for the different sets of sensors. Following the format of fig3 for the TCV case, the poloidal analyses are performed using the low-resolution PP80x and high-resolution H304→H307 sensors on the LFS and the low-resolution I80x sensors on the HFS; the toroidal analyses are performed using solely the low-resolution T00x sensors, then solely the high-resolution H301→H305

sensors, then combining these two sets of sensors. The 2D analyses are performed combining the LFS-only T00x + H30x sensors, and then adding the PP80x and I80x sensors to have an LFS+HFS analysis. For JET, and when excluding the different calibration and noise errors, both SparSpec methods out-performs the LPF method, and the analyses are successful up to very high toroidal and poloidal mode numbers.

However, the situation is not as good as it may appear when considering the actual additional sources of errors due to the differences in the calibration and noise pick-up by the sensors [10]. Figure6c compares the results for the same test $m/n=5/3$ mode used for the TCV analyses as function of frequency, now including these sources of errors. These errors are essentially due to not only ageing of the components (as for TCV), but most importantly to (a) pick-up of EM noise due to sub-optimal cabling connections and grounding schemes between different DAQs accessing the same acquisition line from the in-vessel sensors, which significantly affects the accuracy of the HF magnetic measurements, and (b) the differences in the hardware transfer function cannot be sufficiently well cross-compensated between different sensors over the entire frequency range of the measurements. Above $f_{IN} \sim 50\text{kHz}$ this mode is not anymore sufficiently correctly detected, irrespective of the array and method being used.

5) A synthetic diagnostic for the δB_{MEAS} data: the ITER case.

Figure7 shows the position of the AJ magnetic sensors in ITER, as currently designed (and being installed). The two red ellipses highlight the two groups of sensors used for the toroidal-1D analysis: the bottom group at $\theta \sim -30\text{deg}$ includes high-resolution sensors, the top group at $\theta \sim +30\text{deg}$ does not. Similarly, the blue ellipse at $\phi \sim -140\text{deg}$ includes high-resolution sensors for the poloidal-1D analyses, while the blue ellipse at $\phi \sim -90\text{deg}$ does not. For the concurrent-2D toroidal+ poloidal analyses, both green ellipses include high-resolution sensors, the difference being that one covers a larger toroidal extension.

Figure8(a,b) shows the summary results for the ITER simulations performed for a single $\{n, m\}_{IN}$ mode at $f_{IN}=10\text{kHz}$, with varying $\{n, m, A\}_{IN}$ and running 100 simulations. One specificity of these analyses is that, since the magnetic diagnostic system has not yet been commissioned, only the nominal installation tolerances and input uncertainties on the calibration due to the nominal manufacturing tolerances on all the hardware components can be used, and no data on the noise pick-up is available, therefore the output results appear to be *much better* than those for JET and TCV. Another specificity is that the choice of $f_{IN}=10\text{kHz}$ has only a very minor impact on the results of these simulations since the nominal tolerances for the hardware components in ITER are very strict.

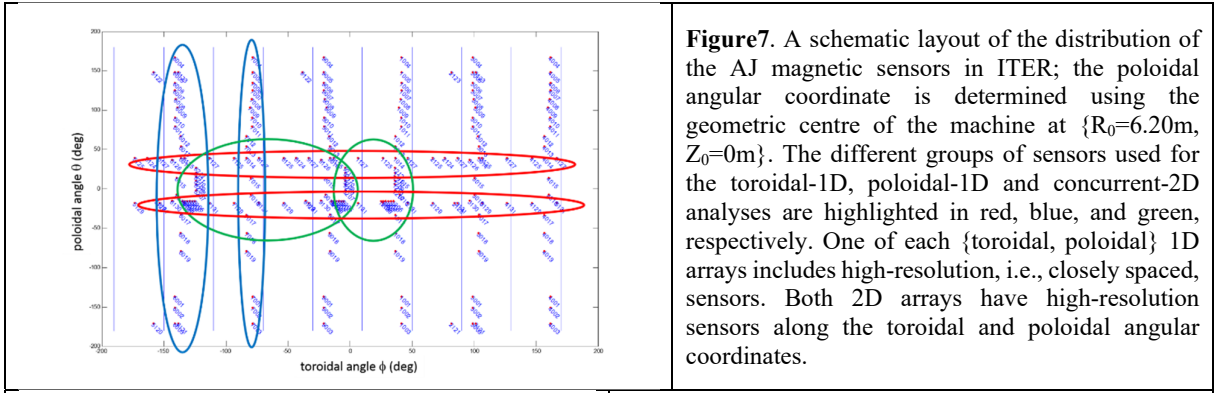


Figure7. A schematic layout of the distribution of the AJ magnetic sensors in ITER; the poloidal angular coordinate is determined using the geometric centre of the machine at $\{R_0=6.20\text{m}, Z_0=0\text{m}\}$. The different groups of sensors used for the toroidal-1D, poloidal-1D and concurrent-2D analyses are highlighted in red, blue, and green, respectively. One of each {toroidal, poloidal} 1D arrays includes high-resolution, i.e., closely spaced, sensors. Both 2D arrays have high-resolution sensors along the toroidal and poloidal angular coordinates.

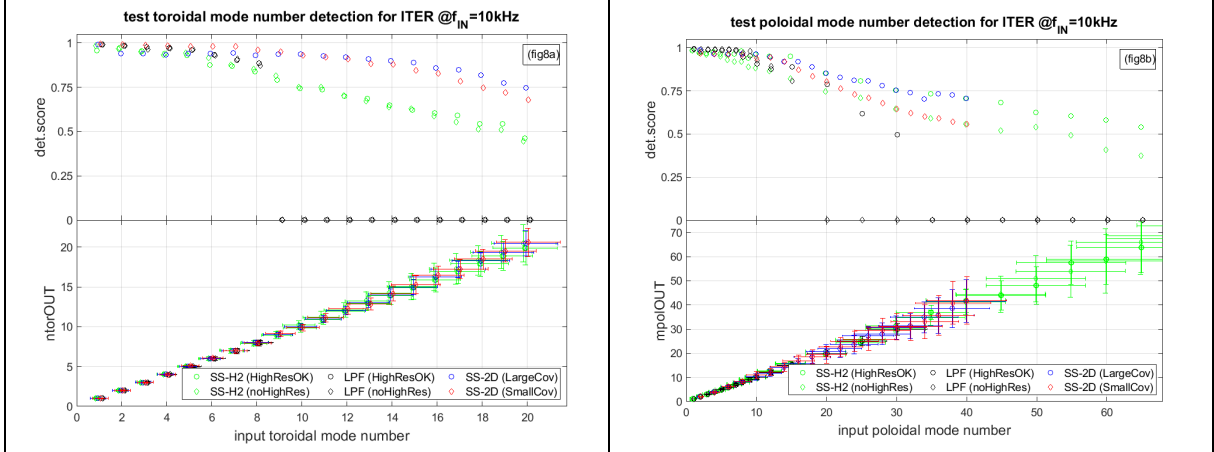


Figure8(a,b). The summary results for the {toroidal, poloidal} mode number detection as function of $\{n, m\}_{IN}$ at $f_{IN}=10\text{kHz}$, using the same format as in fig3(a,b), without considering noise pick-up and calibration. The detection is quite good, particularly for the SparSpec methods, and arrays with high-resolution sensors and larger 2D spatial coverage perform better, particularly for higher mode numbers $\{n, m\}_{IN}>15$. The LPF analysis fails for higher poloidal mode numbers $m_{IN}>20$ even in this idealized case, and thus the SparSpec algorithm should be preferentially used.

For ITER, in the idealized situation where the nominal system specifications are fully respected within the given tolerances for all sensors, we do indeed find that the HF magnetic diagnostic system performs as required by the ITER measurement specifications, even at high mode numbers $\{n, m\}_{IN}>15$ provided the SparSpec 1D and/or 2D algorithms are used.

6) Summary and conclusions.

In this work we have presented the results of end-to-end simulations for a generic HF magnetic diagnostic system, specifically focussing on the existing JET and TCV tokamaks, and on the ITER-AJ subsystem as currently designed and being installed. This analysis provides error bounds and confidence level on the most relevant *observables* (frequency, amplitude, toroidal and poloidal mode numbers) for magnetic fluctuations obtained using different analysis methods (RT and offline) and different arrangements of sensors. Note that it is not intended to run this simulation algorithm on-line for actual RT processing due to its too large computational time requirements. Practically, these values can be tabulated a-priori (namely off-line) and can then be used on-line to inform the action

of the RT control system so that it keeps working within a well-established knowledge basis determined by the measurement accuracy of the diagnostic system being used for RT purposes.

Focusing specifically on the results for the ITER-AJ system simulations and considering solely the idealized case where the nominal system specifications are fully respected within the given (and very strict) tolerances for all sensors, we find that there is an almost perfect detection for all modes up to $\{n, m\}_{IN \sim 25}$ when the SparSpec-1D or SparSpec-2D algorithms are used. The simpler and much faster Linear Phase Fit method fails for poloidal mode numbers $m_{IN} > 20$ even in this idealized case, and thus should not be generally used. This fully satisfies the ITER measurement specifications even for RT analyses.

When comparing the idealized ITER case with the real JET and TCV cases, we find however that the situation is not as optimal as it may seem, particularly when ageing of components is considered, as it is the case for TCV, or where sub-optimal grounding and connection schemes between different DAQs accessing the same acquisition line from the in-vessel sensors are used, as it is the case for JET. In these situations, we find a strong degradation of the overall system measurement performance as function of frequency, because (a) the pick-up of EM noise due to sub-optimal cabling connections and grounding schemes significantly affects the accuracy of the HF magnetic measurements, and (b) the differences in the hardware transfer function cannot be sufficiently well cross-compensated between different sensors over the entire frequency range of the measurements.

As an ongoing work, we are now developing the application of our system simulations to the DTT (most urgently) and DEMO tokamaks, using a GUI framework to facilitate deployment of these tools across potentially interested parties.

Acknowledgements.

This work has been carried out within the framework of the EUROfusion Consortium, funded by the European Union via the Euratom Research and Training Programme (Grant Agreement No 101052200 — EUROfusion). Views and opinions expressed are however those of the author(s) only and do not necessarily reflect those of the European Union or the European Commission. Neither the European Union nor the European Commission can be held responsible for them. This work was also partly supported by the Swiss National Science Foundation.

References.

- [1] D.Testa, *Manufacturing, Installation, Commissioning and First Results with the 3D Low-Temperature Co-fired Ceramic High-Frequency Magnetic Sensors on the Tokamak à Configuration Variable*, Tutorial Paper in Review of Scientific Instruments **91** (2020), 081401; doi: <https://doi.org/10.1063/1.5115004>; look specifically at Section-I in the Supplemental Material.
- [2] C. Galperti et al., *Integration of a Real-Time Node for Magnetic Perturbations Signal Analysis in the Distributed Digital Control System of the TCV Tokamak*, IEEE Trans. Nucl. Sci **64(6)** (2017), 1446; doi: <http://dx.doi.org/10.1109/TNS.2017.2711625>.
- [3] ITER measurement specifications for the HF magnetic diagnostic system: System Design Description (DDD) 55.A0 Magnetic Diagnostics, document 3UYGX, dated 14.09.2015; document available upon request to the corresponding author of this work (duccio.testa@epfl.ch).
- [4] Contract document for the F4E-ITER contract F4E-OPE-0883 for the development of RT software for the analysis of magnetic instabilities in ITER; relevant extracts from this document are available upon request to the corresponding author of this work(duccio.testa@epfl.ch).
- [5] D.Testa et al., *Sparse Representation of Signals: from astrophysics to real-time data analysis for fusion plasmas and system optimization analysis for ITER*, Topical Review paper, Plasma Phys. Contr. Fusion **58** (2016), 123001; doi: <http://dx.doi.org/10.1088/0741-3335/58/12/123001>.
- [6] D.Testa, J.Charrière, *The SparSpec algorithm and the application to the detection of spatial periodicities in tokamaks: from a 1D to a 2D analysis*, Physica Scripta **97** (2022) 115602; doi: <https://doi.org/10.1088/1402-4896/ac95dc>.
- [7] A.N.Kolmogorov, *The local structure of turbulence in incompressible viscous fluid for very large Reynolds numbers*, Dokl. Akad. Nauk. SSSR **30(4)**, 1941; translated and reprinted in the Proceedings of the Royal Society (London), **434** (1991), 9-13.
- [8] J.-M.Moret, F.Buhlmann, D.Fasel, F.Hofmann, G.Tonetti, *Magnetic measurements on the TCV Tokamak*, Review of Scientific Instruments **69** (1998), 2333.
- [9] D.Testa et al., *LTCC Magnetic Sensors at EPFL and TCV: Lessons Learnt for ITER*, Fusion Engineering and Design **146** (2019), 1553; doi: <https://doi.org/10.1016/j.fusengdes.2019.02.127>.
- [10] D.Testa et al, internal reports for the JET T17-03 task, currently unpublished.